

Article

On the Effect of the Nature of Carbon Nanostructures on the Activity of Bifunctional Catalysts Based on Manganese Oxide Nanowires

Nicolás Ignacio Villanueva-Martínez, Cinthia Alegre ^{*}, David Sebastián , Nataly Orozco and María Jesús Lázaro ^{*}

Instituto de Carboquímica–CSIC, Calle Miguel Luesma Castán, 4, 50018 Zaragoza, Spain; nvillanueva@icb.csic.es (N.I.V.-M.); dsebastian@icb.csic.es (D.S.)

^{*} Correspondence: cinthia@icb.csic.es (C.A.); mlazaro@icb.csic.es (M.J.L.)

Abstract: Manganese oxide nanowires (MONW) combined with carbon nanostructures were synthesized using three different carbon materials, and their effect on the activity towards Oxygen Reduction Reaction (ORR) and Oxygen Evolution Reaction (OER) was investigated in alkaline electrolytes. The carbon structures were carbon nanofibers (CNF), multiwall carbon nanotubes (CNT) and reduced graphene oxide (rGO). Both MONW and carbon nanostructures were characterized by X-ray diffraction, scanning and transmission electron microscopy, N₂ physisorption and X-ray photoelectron spectroscopy. The electrochemical activity was assessed in a three-electrode cell. Composite MONW/CNF showed the best activity towards ORR, and MONW/rGO exhibited the highest activity towards OER of the series. The addition of the carbon nanostructures to MONW increased the number of electrons transferred in the ORR, indicating a synergistic effect between the carbon and manganese oxide structures due to changes in the reaction pathway. The analysis of Tafel slopes and electrochemical impedance spectroscopies showed that carbons and MONW catalyze different steps of the reactions, which explains the better activity of the composites. This led us to synthesize a MONW/rGO-CNF composite, where rGO-CNF is a hybrid carbon material. Composite MONW/rGO-CNF showed an improved activity towards ORR, close to the benchmark Pt/C catalyst, and activity towards OER, close to MONW/rGO, and better than the benchmark IrO₂ catalyst. It also showed remarkable stability in challenging operation conditions.

Keywords: bifunctional catalysts; carbon nanostructures; manganese oxide; oxygen reduction; oxygen evolution



Citation: Villanueva-Martínez, N.I.; Alegre, C.; Sebastián, D.; Orozco, N.; Lázaro, M.J. On the Effect of the Nature of Carbon Nanostructures on the Activity of Bifunctional Catalysts Based on Manganese Oxide Nanowires. *Catalysts* **2023**, *13*, 1240. <https://doi.org/10.3390/catal13091240>

Academic Editor: Ermete Antolini

Received: 23 July 2023

Revised: 18 August 2023

Accepted: 24 August 2023

Published: 26 August 2023



Copyright: © 2023 by the authors. Licensee MDPI, Basel, Switzerland. This article is an open access article distributed under the terms and conditions of the Creative Commons Attribution (CC BY) license (<https://creativecommons.org/licenses/by/4.0/>).

1. Introduction

Bifunctional air electrodes have gained increased interest over the last years due to their relevance to sustainable energy devices, including regenerative fuel cells and metal-air batteries [1,2]. These bifunctional air electrodes are responsible for the oxygen evolution reaction (OER) and oxygen reduction reaction (ORR), which are known for their sluggish kinetic reactions due to the complex $4e^-$ mechanisms governing them [3,4]. Noble metals such as Pt/C and IrO₂ or RuO₂ have been widely studied and are considered the most active catalysts for ORR and OER, respectively. However, these catalysts are not bifunctional: Pt shows very poor activity towards OER, and neither IrO₂ nor RuO₂ are active for the ORR [5,6]. Amongst noble metals, Pd displays high activity towards both reactions [7–9], but its cost is even higher than that of Pt, a reason that encourages the search for another kind of catalyst.

In the last decade, great efforts have been devoted to the search for bifunctional catalysts based on non-noble transition metals. Cobalt-based catalysts, either in the form of spinels, perovskites or mixed oxides, are reported as the most active bifunctional catalysts for ORR and OER [10–13]. However, due to the increased use of lithium-ion batteries, cobalt

has become a critical raw material, not being interesting from an economic or ethical point of view. This fact has motivated the quest for alternative catalysts based on non-critical raw materials, such as Fe, Ni or Mn.

Some reviews have reported interesting performances towards ORR and OER for manganese-based catalysts. Manganese oxides exist in different oxidation states (MnO , Mn_3O_4 , Mn_2O_3 , MnO_2 , MnOOH) and nanostructures (cubic [14], layered [15], spinels [16], etc.). Among them, nanowires have been reported as efficient nanostructures providing high activity for the electrocatalysis of oxygen reactions due to their structure favoring cavities with MnO_6 octahedra disposed on the edge and corner-linked [17,18].

One challenge concerning not only manganese oxides but transition metal-based catalysts in general, is their low electrical conductivity [19]. To overcome this issue, transition metal-based catalysts are generally mixed with carbon materials. Several studies have reported the use of manganese oxide combined with diverse carbon materials, from graphene-based materials to carbon nanotubes/carbon nanofibers, mesoporous carbons doped with heteroatoms, etc. For example, catalysts like Ni-MnO over graphene aerogel [20], Co/Mn oxide intertwined with carbon nanotubes [21] and Pd-MnO₂/carbon nanotubes [22] have achieved bifunctionalities (differences between the potentials for OER and ORR) in the 0.8–0.9 V range. Poux et al. synthesized La-Sr-Mn perovskites/pyrolytic carbon composites [23] and concluded that carbon not only increases the electrical conductivity of the catalyst but also increases the surface area and favors oxygen adsorption, thus enhancing ORR. In a previous work [24], we observed that combining iron-doped manganese oxide nanowires with carbon nanofibers generated a synergistic effect that was ascribed to both an increase in the conductivity of the catalyst and to enhanced oxygen adsorption, eventually favoring ORR.

In the last years, several studies have achieved good activities for OER and ORR using manganese oxides and carbon materials in combination. For example, He et al. [25] synthesized MnO_x /carbon nanotubes composites that showed bifunctional potential difference (between the OER potential at 10 mA cm^{-2} and the ORR half-wave potential) of 0.91 or 0.92 V and onset potentials for ORR of 0.83 or 0.84 V vs. RHE and for OER of 1.54 V or 1.58 V vs. RHE, depending on the oxidation state of Mn. Their Tafel slopes ranged between 83 and 114 mV dec^{-1} for ORR. Other studies with doped manganese oxides and doped carbon nanostructures show interesting results. One case is the catalyst developed by Niu et al. [26], who combined Co-doped MnO and N-doped carbon nanowires to obtain a highly active catalyst for both OER and ORR. The onset potentials, respectively, were 1.46 and 0.96 V vs. RHE, respectively. They also obtained a half-wave potential for ORR of 0.85 V vs. RHE and a potential for 10 mA cm^{-2} in OER of 1.49 V vs. RHE, totalizing 0.64 V of bifunctional gap difference. Their co-doped material even achieved Tafel slopes low as 74 and 53 mV dec^{-1} for ORR and OER, respectively.

Studies assessing manganese oxides with carbon materials usually evaluate one individual species, so there is not a straightforward comparison nor a proper evaluation of the effect of the carbon material on the activity of manganese-based catalysts. For this reason, the present manuscript investigates the performance of manganese oxide in the form of nanowires (the most active proven structure for ORR/OER) combined with three carbon nanostructures: carbon nanofibers, carbon nanotubes and reduced graphene oxide, assessing how these carbon materials affect the activity for OER and ORR of manganese oxide nanowires. In addition, a carbon hybrid structure, graphene nanofibers, is proposed in order to maximize the activity of the manganese oxide nanowires, taking advantage of the main properties of the individual carbon nanostructures.

2. Results

2.1. Physical-Chemical Characterization

TEM micrographs (Figure 1) allowed us to study the arrangement and morphology of the carbon nanostructures. CNFs (Figure 1a) have micron-size lengths and diameters around 50 nm, with a fishbone morphology (Figure 1d). CNTs (Figure 1b,e) have wider

diameters, ca. 60–70 nm, and are shorter than CNFs but still have lengths longer than 1 μm . CNTs are multiwall type, as can be seen in Figure 1e. In addition, graphitic carbon particles around the iron catalyst can also be observed. rGO shows the typical sheet-like morphology, as shown in Figure 1c,f, where single sheets can be observed, presenting wrinkles, which are a product of the defects that are produced during the graphene oxide thermal reduction [27,28]. Figure S1 (Supporting Information, Section S1) shows SEM and TEM micrographs of MONW. The manganese oxide nanowires have square cross-sections and widths ranging between 60 and 100 nm. Their length can reach up to several microns. TEM and SEM micrographs of the composites (Figure 1g–i) show the good mixing between the phases, with several contact points between the carbon materials and MONW.

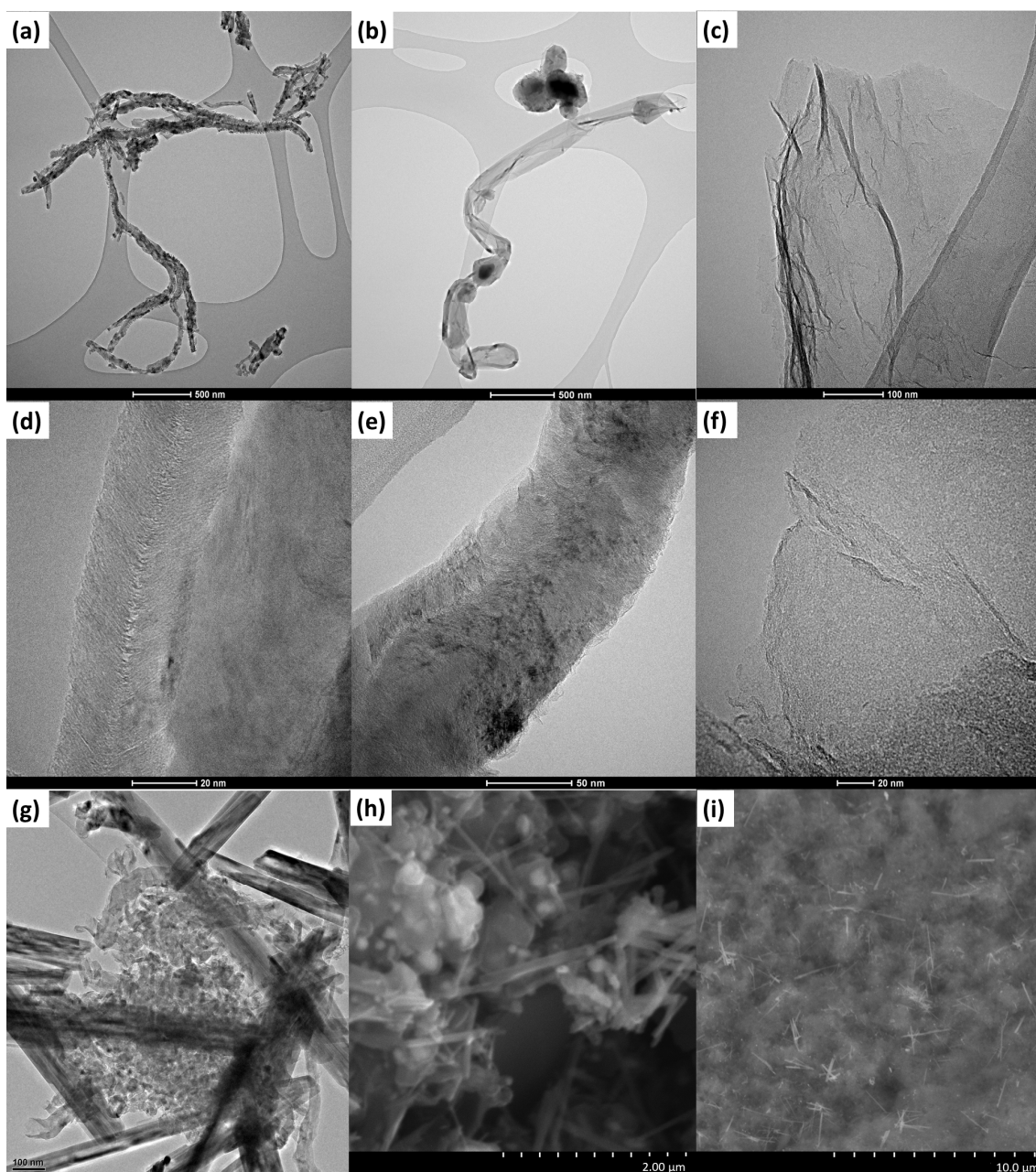


Figure 1. TEM micrographs of CNF (a,d), CNT (b,e), rGO (c,f) and composite MONW/CNF (g). SEM images of composites MONW/CNT and MONW/rGO (h,i).

XRD analyses (Figure 2a) revealed the crystalline structure of the carbon materials. CNF and CNT show a highly graphitic structure, with the characteristic peak of graphite

(JCPDS 75-2078) at $2\theta = 26.5^\circ$ and 26.6° , respectively, attributed to the (002) reflection. These values indicate interplanar distances of 0.337 and 0.335 nm and graphitization degrees of 80% and 100%, respectively. In the case of rGO, the interplanar distance is much higher, 0.347 nm (position of the peak at 25.65°), mainly due to the presence of oxygen functional groups, as can be interpreted from the 5 wt% of oxygen content in this sample (Table 1). Still, this value is far from the typical 0.8–0.9 nm layer separation distance of graphene oxide [29–31], and no peak at $2\theta = 10^\circ$ was observed. The position of the peak agrees with others reported in the literature [32,33]. Other peaks ascribed to graphitic carbon are (100) in the three carbon materials and (004) in CNF and CNT [30]. The (004) peak is not visible in rGO due to its low number of layers. Carbons CNF and CNT also show reflection planes characteristic of the catalyst metals. In CNF, planes (111) and (200) at 44.5° and 51.8° , respectively, corresponding to metallic nickel (JCPDS 04-850) are also observed [34], while CNT shows peaks ascribed to (110) and (200) metallic iron (JCPDS 06-0696) [35], but also to martensite, an iron–carbon alloy (JCPDS 04–003-1419) [36].

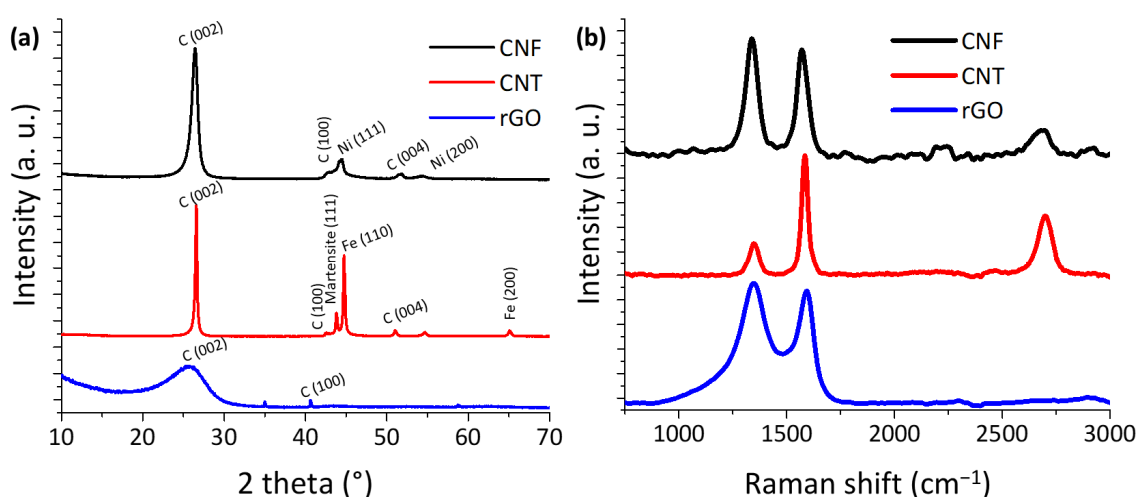


Figure 2. (a) X-ray diffractograms and (b) Raman spectra of the carbon materials.

Table 1. Chemical composition and textural properties of the carbon materials.

Material	Chemical Composition (wt%)				Textural Properties	
	Carbon	Oxygen	Iron *	Nickel *	S_{BET} ($\text{m}^2 \text{g}^{-1}$)	V_{pore} ($\text{cm}^3 \text{g}^{-1}$)
CNF	92.5	-	-	7.3	95	0.24
CNT	76.5	-	23.5	-	11	0.04
rGO	92.9	5.6 **	-	-	175	0.70

* Iron and nickel percentages determined by ICP. ** Oxygen content for rGO determined from EA.

The number of layers comprising carbon nanotubes and reduced graphene oxide was determined by applying Scherrer's equation to the (002) peak. The crystallite size (in the 002 direction) of CNT is approximately 34 nm, which allows us to estimate that carbon nanotubes have 100 layers (or walls), in agreement with TEM micrographs, as the crystallite size calculated by XRD approximately corresponds to the radius of multiwall carbon nanotubes. rGO presents an average crystallite size of 15 nm, corresponding to 4.5 layers, also in good agreement with the TEM micrographs. XRD analysis of MONW is presented in Figure S2 (Section S1). The only present phase is $\alpha\text{-MnO}_2$, and the crystallite size obtained by applying Scherrer's equation to the main peak (211 planes at 37°) is 37 nm. The reflection planes were obtained from JCPDS ($\alpha\text{-MnO}_2$, 00–044–0141) and matched other works found in the literature [37]. MONW were also analyzed using X-ray photoelectron spectroscopy (Figure S3). Mn2p spectra show two $2p_{3/2}$ peaks, at 642.0 eV, ascribed to Mn^{4+}

in MnO_2 ($\approx 88\%$) [38], and at 644.3 eV, ascribed to Mn^{6+} in K_2MnO_4 ($\approx 12\%$) [39]. The O1s orbital can be decomposed into two peaks: one at 539.5 eV, corresponding to lattice oxygen ($\approx 65\%$), and another one at 531.1 eV, ascribed to adsorbed oxygen or water ($\approx 35\%$) [40].

Raman spectroscopy (Figure 2b) was used to investigate the structural defects of the carbon nanostructures. All of them show the characteristic G band: CNF at 1570 cm^{-1} , CNT at 1585 cm^{-1} and rGO at 1593 cm^{-1} . The D band, associated with defects, mainly sp^3 carbon atoms, is also visible in the three samples, being especially intense in CNF and rGO, with I_D/I_G ratios of 1.1 and 1.4, respectively, while CNT has a much smaller amount of defects as can be inferred from its I_D/I_G ratio = 0.4. CNF and CNT also exhibit the 2G band at 2681 and 2700 cm^{-1} , respectively, whereas this band is not visible in rGO due to its low amount of layers. The intensity of the 2G band is especially high in CNT because of the high number of layers.

Elemental analysis and ICP were used to investigate the composition of the carbon materials. CNFs are comprised of 92 wt% carbon and 7 wt% nickel, which is consistent with the catalytic decomposition of methane. An amount of 300 mg of $\text{NiCuAl}_2\text{O}_3$ catalyst yielded approximately 3 g of CNF, indicating that the amount of catalyst should be less than 10 wt% in the final material. CNT, on the other hand, presents a higher amount of metal, around a quarter of the total weight of the sample. Indeed, 300 mg of iron oxide yielded ca. 1.2 g of CNT. rGO has a C:O mass ratio of 17 (atomic ratio of 22), indicating a good—but not complete—reduction of the graphene oxide.

The textural properties of the different carbon nanostructures were studied using nitrogen physisorption (Figure 3, Table 1). All isotherms (Figure 3a) show a hysteresis cycle—type IIb or IV according to the IUPAC classification—characteristic of small particles or crystal aggregates with mesopore-size voids between them [41]. The surface area was calculated with the Brunauer–Emmett–Teller (BET) model (Table 1), being $175\text{ m}^2\text{ g}^{-1}$, $95\text{ m}^2\text{ g}^{-1}$ and $11\text{ m}^2\text{ g}^{-1}$ for rGO, CNF and CNT, respectively. The low surface area of CNT is explained by the graphitic carbon particles formed together with the nanotubes, the high number of walls of the tubes and the large amount of iron in this sample. The textural characteristics of MONW are displayed in Figure S4 (Section S1, in the Supplementary Materials). MONW also present a type IV adsorption isotherm, indicative of mesoporosity, with a surface area of $23\text{ m}^2\text{ g}^{-1}$ and a pore size distribution, including meso- and macropores.

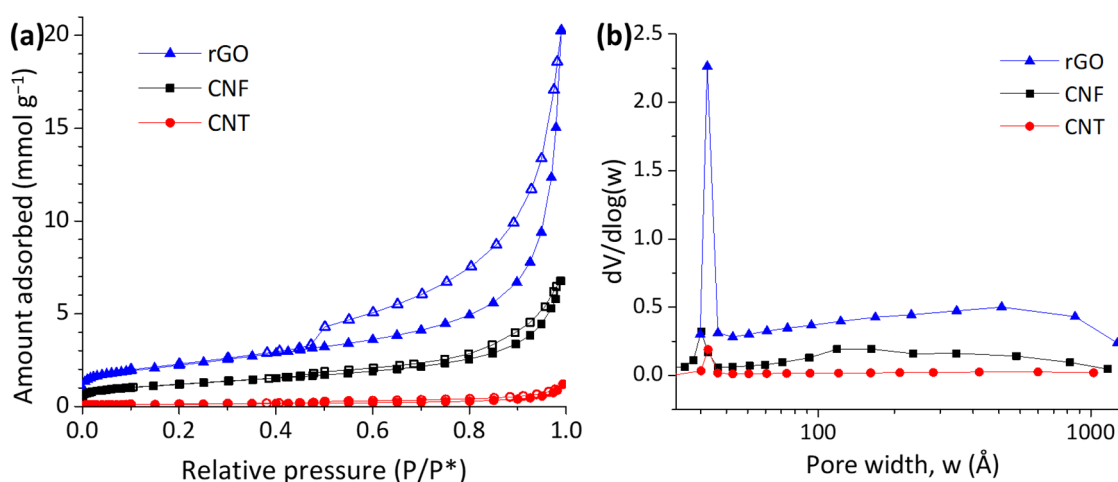


Figure 3. Nitrogen physisorption isotherm (a) and BJH (Barrett–Joyner–Halenda Model) pore size distribution (b) of the carbon materials.

Pore size distributions were obtained by applying the BJH method to the desorption branch of the isotherms, revealing that carbon nanostructures present pores in the 4–5 nm range. Consistently with the pore size distribution and surface areas, rGO has the highest pore volume of all samples, $0.70\text{ cm}^3\text{ g}^{-1}$, followed by $0.24\text{ cm}^3\text{ g}^{-1}$ of CNF and $0.04\text{ cm}^3\text{ g}^{-1}$

of CNT. CNF and rGO also display a small fraction of microporosity, with micropore areas of 17 and 29 $\text{m}^2 \text{g}^{-1}$, respectively, and micropore volumes of 0.009 and 0.017 $\text{cm}^3 \text{g}^{-1}$.

2.2. Effect of the Carbon Nanostructure on the Catalytic Activity towards the Oxygen Reduction and Evolution Reactions

Linear sweep voltammeteries (Figure 4) performed in the ranges 1.2–0.2 V for ORR and 1.1–1.8 V vs. RHE for OER were carried out to investigate the catalytic activity of MONW/C composites, alongside evaluating their reversibility towards ORR/OER. Table 2 collects the main electrochemical parameters derived from the LSV curves, such as the onset potential for both ORR and OER ($E_{\text{ORR, onset}}$ being the potential at -0.1 mA cm^{-2} current density and $E_{\text{OER, onset}}$ the potential at 1 mA cm^{-2} current density), half-wave potential for the ORR ($E_{1/2}$), the limiting current density (j_d), the number of exchanged electrons for the ORR (n), the potential for the OER at 10 mA cm^{-2} (E_{10}) and the potential gap between ORR and OER.

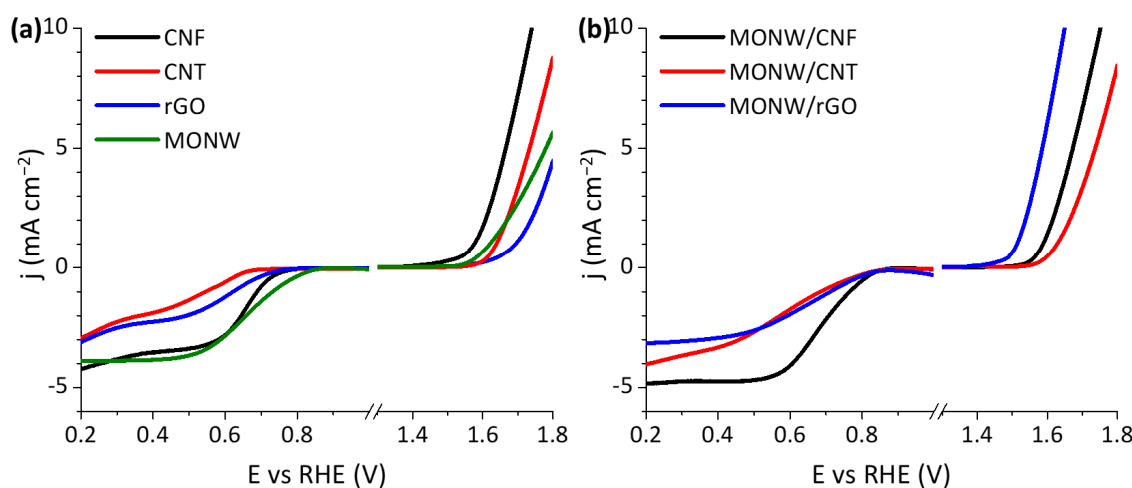


Figure 4. ORR and OER LSVs over (a) carbon materials and manganese oxide; (b) composite MONW/C catalysts. Experiments were carried out on an RDE at 1600 rpm.

Table 2. Electrocatalytic parameters obtained for the individual carbon nanostructures and for MONW/C composites.

Catalyst	Oxygen Reduction Reaction				Oxygen Evolution Reaction		Reversibility ORR/OER
	$E_{\text{ORR, onset}}$ (V vs. RHE)	j_d (mA cm^{-2})	$E_{1/2}$ (V vs. RHE)	n	$E_{\text{OER, onset}}$ (V vs. RHE)	E_{10} (V vs. RHE)	ΔE^* (V)
CNF	0.78	−4.23	0.66	2.9	1.58	1.74	1.08
CNT	0.68	−2.90	0.48	2.9	1.64	1.82	1.34
rGO	0.76	−3.06	0.57	3.0	1.69	1.92	1.35
MONW	0.84	−3.89	0.66	2.7	1.62	1.90	1.24
MONW/CNF	0.85	−4.84	0.69	3.4	1.59	1.75	1.06
MONW/CNT	0.82	−4.02	0.57	3.8	1.63	1.83	1.25
MONW/rGO	0.83	−3.15	0.64	3.4	1.51	1.65	1.01

* ΔE was calculated by subtracting the half-wave potential for the ORR from the potential at 10 mA cm^{-2} for the OER ($\Delta E = E_{10} - E_{1/2}$).

Figure 4a reveals that CNF (without MONW) is the most active carbon material for both the OER and the ORR, with a similar LSV for the ORR to the individual MONW. This excellent catalytic behavior is due to the presence of nickel in the CNF, an active metal towards both ORR and OER, alongside the outstanding electrical conductivity of the carbon

material. In a previous work [24], we showed that acid-leached carbon nanofibers also hold a considerable, yet slightly lower, catalytic activity towards ORR and non-negligible activity towards OER. As was discussed in Section 2.1, CNF, although still presenting a small amount of nickel (<2 wt%), has a large amount of structural defects, which have been reported as active sites [42]. This is consistent with what has been reported in the literature regarding acid-leached carbon nanofibers showing activity for ORR and OER [43,44]. CNT also shows a decent OER activity due to the presence of Fe; however, its performance towards the ORR is the lowest of the series, which could be due to the low amount of defects (acting as active sites for ORR) since this sample is the most graphitic one. Acid-leached CNTs were tested to assess the activity of the carbon nanostructure (Figure S5). It can be observed that the activity towards ORR barely reduces, while the activity towards OER shows a more significant decrease in activity, with the onset overpotential increasing 66 mV. The mild effect of leaching on the activity of CNT can be explained by the encapsulation of Fe particles in a graphitic matrix under a high number of layers (as explained by XRD and seen in TEM), which does not allow them to act as catalytic active sites. This is why other iron-over-carbon catalysts in the literature show better activities towards OER [45] or ORR [46]. rGO shows the lowest ORR/OER performance on its own. On the other hand, the catalytic activity of MONW without any carbon material is good for the ORR but not for the OER, highlighting the need for a carbon nanostructure to maximize the catalytic activity of Mn oxide sites by enhancing the electrical conductivity. The onset potentials for the ORR follow the trend $CNT < rGO < CNF < MONW$, and for the OER, the trend is $rGO > CNT > MONW > CNF$.

Upon combination of MONW with the different carbon nanostructures (Figure 4b), there is a clear improvement in the catalytic activity of the individual manganese oxide nanowires, as can be ascertained from both the parameters displayed in Table 2 and the curves of Figure S6 in the Supporting Information (Section S2.1), comparing each MONW/C composite with its individual components. This highlights the importance of adding carbon for an enhanced activity for the oxygen evolution reaction. On the other hand, for the ORR, there is only a synergistic effect between Mn and C in the case of using CNF. Neither the combination of MONW with rGO nor with CNT provides a more active catalyst, which could be ascribed to a worsened interaction between these carbonaceous materials with the metal oxide active phase. As previously explained, CNT possesses a highly graphitic character and a low surface area, which could hinder the carbon–metal interaction. On the other hand, in the case of MONW/rGO, its low performance for the ORR might be explained by the large difference in surface area between carbon and manganese oxide phases. As the surface area of reduced graphene oxide is approximately seven times greater than that of the manganese oxide nanowires, most of the exposed area of the catalyst is rGO and not MONW. The poor mixing between the two materials can be seen in the SEM micrograph displayed in (Figure 1i).

In general, the electrochemical parameters shown in Table 2 reveal a positive shift of the onset potential for the ORR between 70 and 150 mV and between 30 and 90 mV for the half-wave potential for the MONW/C composites with respect to the individual carbon nanostructures.

Comparing the activity of the composite catalysts (MONW/C: CNF, CNT and rGO in Figure 4b), both MONW/CNF and MONW/rGO show an excellent OER activity, and MONW/CNF also exhibits an outstanding ORR performance. The MONW/CNT composite is the least active one for both ORR/OER, probably due to a worsened interaction between Mn and C due to the lower surface area of CNTs, the low amount of defects, and we cannot discard some effect due to the encapsulation of the iron particles with the carbon matrix.

The synergistic effect between C and MONW for the OER is also reflected in the improvement of the ΔE value, around 70 to 200 mV lower for the MONW/C composites than for the individual components. This reveals that adding carbon to manganese-based catalysts is a good strategy to improve the reversibility of systems operating on ORR/OER.

Both MONW/rGO and MONW/CNF show the lowest values of ΔE (1.01 and 1.06 V, respectively), mainly due to their superior performance towards OER (lower E_{10}). The composite MONW/CNT has the highest ΔE of all the composites, as it presents the lowest activities towards both ORR and OER.

The number of exchanged electrons for the ORR was assessed by applying the Koutecky–Levich (K-L) approach in the diffusional limit of the LSVs performed at different rotation speeds (400, 625, 900, 1600 and 2500 rpm). Further details can be found in the Supporting information (Section S2.3, Figures S7 and S8). The K-L plots for both carbon nanostructures and composites (MONW/C, C: CNF, CNT, rGO) are shown in Figure 5, and all the electrochemical parameters obtained from the LSVs are gathered in Table 2. CNF, CNT, rGO and MONW exhibit the exchange of ca. 3 electrons in the diffusional limit of ORR (2.9, 2.9, 3.0 and 2.7, respectively), indicating that oxygen is reduced to both hydroxide and peroxide. Despite not having the highest number of electrons transferred, CNF is more active than the other materials in the diffusional limit, as is corroborated by the intercept on the Y-axis at a lower value (higher kinetic current at 0.2 V vs. RHE). The superior performance of nanofibers can be explained by their physical-chemical properties: the presence of nickel from the catalyst [24], their relatively high surface area and the amount of structural defects acting as active sites [42].

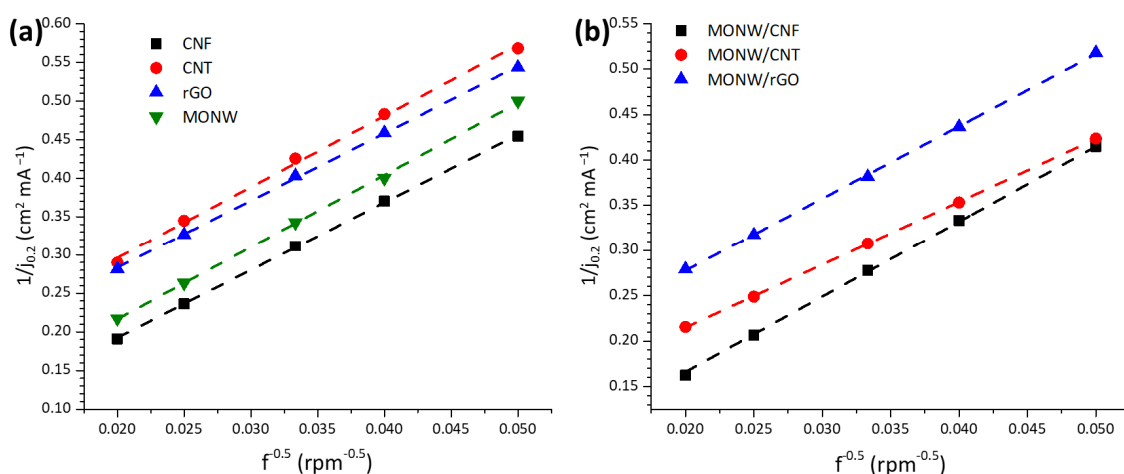
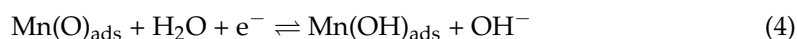
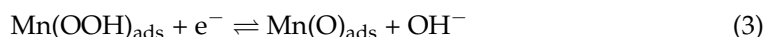
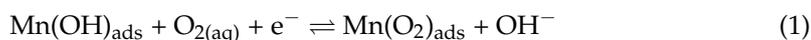


Figure 5. Koutecky–Levich plots at $E = 0.2$ V vs. RHE of (a) carbon materials and manganese oxide and (b) composite catalysts.

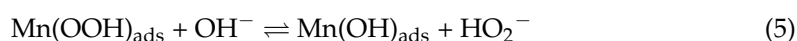
MONW/C composites exhibit a higher number of exchanged electrons than the individual carbon materials. The largest synergistic effect in terms of transferred electrons is observed in the composite MONW/CNT, as it exhibits 3.8 transferred electrons. This number, however, must be analyzed cautiously, as the LSV at 1600 rpm (Figure 4b) suggests the diffusional limit has not yet been reached at 0.2 V. In the case of MONW/CNF and MONW/rGO, the number of electrons is slightly lower, with 3.4, meaning 70% of hydroxide formation. However, the high intercept of the MONW/rGO curve with the Y-axis (Figure 5b, blue triangles) indicates a low intrinsic current density at 0.2 V vs. RHE, only 8.4 mA cm^{-2} , which is due to the poor interaction between the carbon phase and the metallic phases, as previously explained.

Two paths have been described in the literature for oxygen reduction over manganese catalysts [47]. The first mechanism is the four-electron reaction that yields OH^- . Since the surface of metal oxide electrodes in a strongly alkaline medium is covered by adsorbed OH species [48,49], the first step involves the displacement of OH to adsorb one O_2 molecule with the acceptance of one electron (Equation (1)). The adsorbed OO is then protonated (Equation (2)), and after that, a hydroxide anion is released, and a single oxygen atom

remains adsorbed (Equation (3)). Finally, the adsorbed oxygen is protonated to obtain a hydroxyl group adsorbed to the manganese oxide (Equation (4)).



Oxygen can also be reduced to peroxide in a two-electron pathway. The first two steps are the same as in the four-electron mechanism (Equations (1) and (2)). The adsorbed peroxy then desorbs as hydroperoxide and is replaced by hydroxide (Equation (5)). This happens because the energy is not enough to break the O=O bond.



The peroxide can degrade non-electrochemically to water and oxygen (Equation (6)) or react electrochemically with another adsorbed OH group to yield adsorbed oxygen and 2 hydroxide ions (Equation (7)) and then reduce to hydroxide following equation Equation (4), completing a “2 + 2” mechanism. The difference between the four-electron and the 2+2 electron pathways is that the first one is dissociative, and the latter is associative.



In both mechanisms, the rate-determining step is the electrochemical adsorption of oxygen. In fact, in a previous work [24], we showed that the ability of manganese oxide to adsorb oxygen plays a key role in the ORR kinetics. The four-electron and the two-electron pathways compete, as the operation potentials are lower than the standard reduction potentials for the two mechanisms (1.23 V vs. RHE and 0.77 V vs. RHE, respectively). As a result, the number of electrons is between 2 and 4 (2.7 in MONW at 0.2 V vs. RHE). By operating at a less negative potential, i.e., calculating the number of exchanges by the Koutecky–Levich method at 0.4 V vs. RHE, it increases to 3.7 (Figure S9, Section S2.3). This happens because the overpotential is too low for the 2-electron pathway. As the standard potential for peroxide reduction in alkaline electrolyte is 1.71 V vs. RHE, the potentials at which the number of electrons are calculated (either 0.2 or 0.4 V vs. RHE) should imply a rapid reduction of the peroxide if it re-adsorbs. Consequently, the amount of hydroperoxide that reduces to hydroxide does not depend on the potential—but, rather, on the rates at which hydroperoxide degrades into oxygen (Equation (6)) and at which it re-adsorbs on the catalyst.

The activity of the catalysts was also assessed by analyzing Tafel slopes for both ORR and OER. Further details can be obtained in the Supporting Information. To obtain the Tafel slopes in ORR, the intrinsic current density was estimated using the Koutecky–Levich method (Equation S1 in Supporting information). The effective overpotential (η_{eff}) was calculated according to Equation (8):

$$\eta_{\text{eff}} = E - E^0 - IR \quad (8)$$

where E is the measured potential, E^0 is the standard potential at the electrolyte concentration (1.23 V vs. RHE), I is the measured current, and R is the electrolyte resistance, calculated using Newman’s equation [35]. Figure 6 shows the Tafel slopes obtained for ORR (Figure 6a) and OER (Figure 6b) for the MONW/C composites, and Figure S10 (Section S2.4 in the Supporting Information) shows the Tafel slopes for the individual components,

carbon nanostructures and MONW. The Tafel parameters for all the catalysts are collected in Table 3.

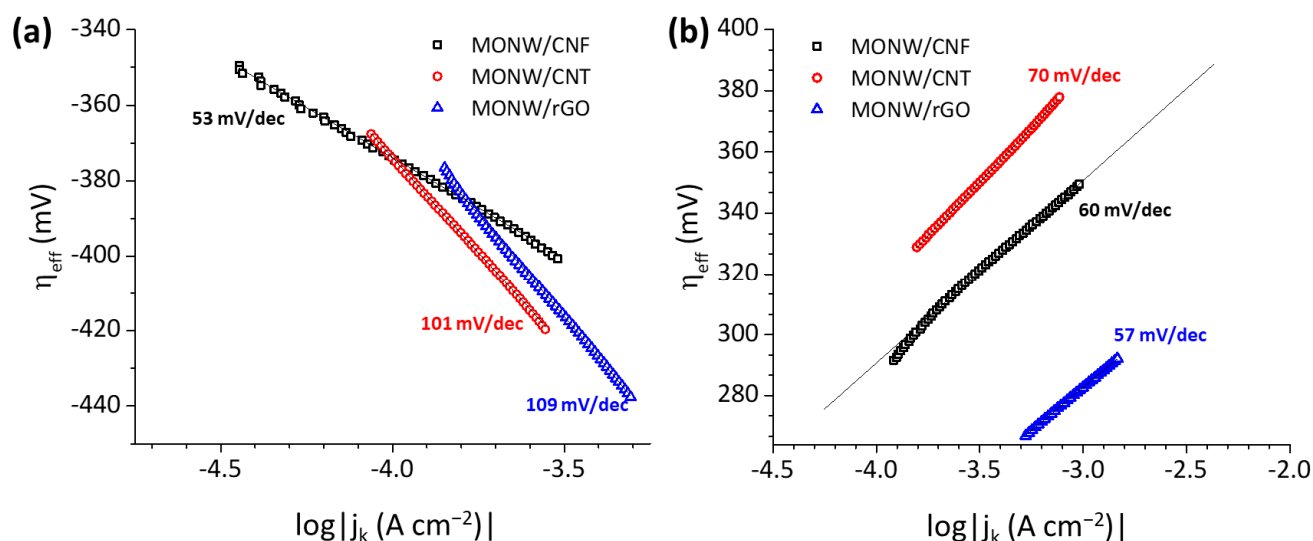


Figure 6. ORR (a) and OER (b) Tafel plots of composite catalysts. Experiments carried out over a RDE at 1600 rpm.

Table 3. Kinetic parameters obtained from the Tafel slopes for the different catalysts.

Catalyst	Oxygen Reduction Reaction		Oxygen Evolution Reaction	
	j_0 (mA cm ⁻²)	Tafel Slope (mV dec ⁻¹)	j_0 (mA cm ⁻²)	Tafel Slope (mV dec ⁻¹)
CNF	1.8×10^{-10}	76	1.7×10^{-4}	87
CNT	6.8×10^{-11}	88	8.5×10^{-6}	38
rGO	3.5×10^{-10}	86	4.3×10^{-4}	131
MONW	4.9×10^{-10}	136	1.0×10^{-5}	73
MONW/CNF	9.1×10^{-9}	53	1.4×10^{-6}	60
MONW/CNT	2.0×10^{-8}	101	3.3×10^{-6}	70
MONW/rGO	4.8×10^{-8}	109	1.0×10^{-5}	57

The superior performance of MONW/CNF for the ORR is also evident in its low Tafel slope, 53 mV dec⁻¹, while MONW/CNT and MONW/rGO exhibit approximately double that value (ca. 100 mV dec⁻¹). The synergistic effect between CNF and MONW can be appreciated in the composite having a lower Tafel slope than the materials on their own. In the case of OER, the three composites have similar Tafel slopes, ranging from 57 to 70 mV dec⁻¹. However, the MONW/rGO composite has an exceptional exchange current density (j_0) of 1.0×10^{-5} mA cm⁻², one order of magnitude higher than the 1.4×10^{-6} mA cm⁻² of MONW/CNF and the 3.3×10^{-6} mA cm⁻² corresponding to MONW/CNT. When analyzing the Tafel slopes of the carbon materials, it is possible to observe that the exchange current density of rGO for OER is 4.3×10^{-4} mA cm⁻², a higher value than the rest of the catalysts. This suggests that reduced graphene oxide provides the largest surface where the OH⁻ anions can adsorb and then be oxidized over the manganese oxide nanowires.

Tafel slopes also provide information about the mechanism of the reactions and are closely related to the kinetics [50], especially to the rate-determining steps of ORR and OER. As previously stated, in Mn-based catalysts, the rate-determining step for ORR is assumed to be the hydroxide-displacement oxygen adsorption. In fact, the obtained 136 mV dec⁻¹ in MONW is close to the theoretical 120 mV dec⁻¹ calculated as the Tafel slope when the first electron transfer is the rate-limiting step [51]. In contrast, carbon materials studied

in this work show ORR Tafel slopes closer to 60 than to 120 mV dec^{-1} (especially CNF, Figure S10), suggesting that the rate-limiting step is the protonation of adsorbed O_2^- rather than the first electron transfer [51,52]. This way, catalyst MONW/CNF, for example, has two phases that are able to catalyze different steps of the reaction pathway, explaining its better performance than the separate phases. In the case of OER, the reverse of the four-electron ORR pathway was considered as the predominant mechanism (inverse of Equations (1)–(4)). The Tafel slope of MONW (73 mV dec^{-1}) suggests that the third step (inverse of Equation (2)) is the rate-limiting step on this material [53]. In rGO, on the other hand, the Tafel slope of 131 mV dec^{-1} suggests that the first step, i.e., the protonation of an adsorbed hydroxyl group (inverse of Equation (4)), which has a theoretical Tafel slope of 120 mV dec^{-1} [54]. As in the case of ORR, the different phases show the ability to catalyze different steps of the reaction pathway.

2.3. Catalytic Activity towards the Oxygen Reduction and Evolution Reactions for a Composite Material between Mn Oxide and Hybrid Carbon Nanostructure

Taking into account that the composite catalyst based on CNF (MOWN/CNF) was the most active towards ORR while the one based on rGO (MONW/rGO) was the most active towards OER, hybrid carbon materials composed of rGO and CNF were investigated, aimed to take advantage of both carbon nanostructures towards an enhanced MONW/C catalyst.

Two synthetic strategies were evaluated to obtain the hybrid carbon material. The first strategy consisted of mechanical mixing of the two carbon nanostructures CNF and rGO (25 wt% CNF and 25 wt% rGO) with 50 wt% MONW. This process yielded a material named MONW/mm[rGO-CNF] that, just like the three original composites, was comprised of 50% carbon material and 50% manganese oxide nanowires and tested in the same conditions as the others. However, this strategy was not successful since the catalytic activity for ORR and OER was not remarkable, as can be seen in the Supporting Information (Figure S11, Section S2.5 in Supporting Information).

The second strategy consisted of synthesizing a hybrid carbon material by growing carbon nanofibers in an rGO matrix (rGO-CNF) in order to obtain an intimate mixture at the nanoscale of the two carbon phases. To do so, nickel nanoparticles, acting as CNF growth sites, were deposited on rGO, which was subsequently treated in a CH_4 atmosphere, following a similar method to the one reported in a previous work [55]. TEM images of this hybrid carbon are shown in Figure 7, where the presence of irregular nanofilaments is advised together with an amorphous carbon phase from rGO. At high magnification (Figure 7b), the graphitic layers corresponding to the nanofilaments can be clearly observed, which follow a platelet structure with an irregular surface. This hybrid rGO-CNF presents a BET surface area of 380 $\text{m}^2 \text{g}^{-1}$, much higher than the individual counterparts (95 $\text{m}^2 \text{g}^{-1}$ for CNF and 175 $\text{m}^2 \text{g}^{-1}$ for rGO, see Table 1), as a result of the separation of graphenic layers from rGO due to the intercalation of nanofilaments. Figure 7c shows a SEM image of the composite MONW/CNF-rGO, where a good contact between the carbon and MnO_2 phases is visible, with manganese oxide nanowires inserted between the carbon nanofibers.

To produce the catalyst, the rGO-CNF hybrid material was mixed in a planetary mill with manganese oxide nanowires in a 1:1 mass ratio following the same procedure as the other carbon materials. The composite material was named as MONW/rGO-CNF. Figure 8 shows the LSVs of the hybrid carbon composited with manganese oxide, compared to MONW/rGO and MONW/CNF, and with benchmark catalysts for ORR and OER: Pt supported on carbon, and IrO_2 , respectively.

The most remarkable result is that the catalyst MONW/rGO-CNF presents an improved activity for the ORR compared to CNF- and rGO-supported MONW. The number of exchanged electrons is higher, 3.7 (see Table 4), and the onset and half-wave potentials are more than 50 mV more positive than the other MONW/C catalysts.

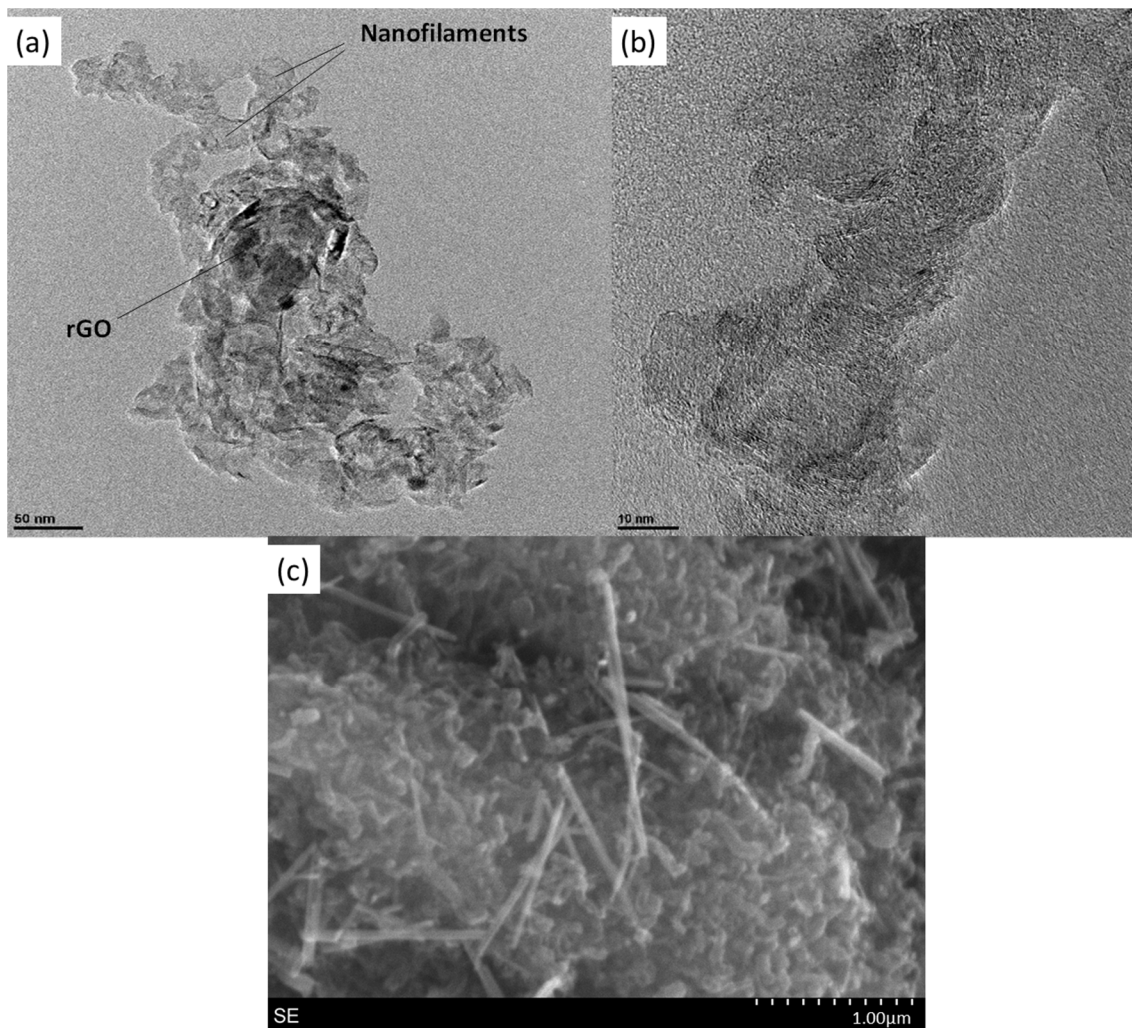


Figure 7. TEM (a,b) and SEM (c) micrographs of rGO-CNF composite produced by growing CNF on the surface of rGO.

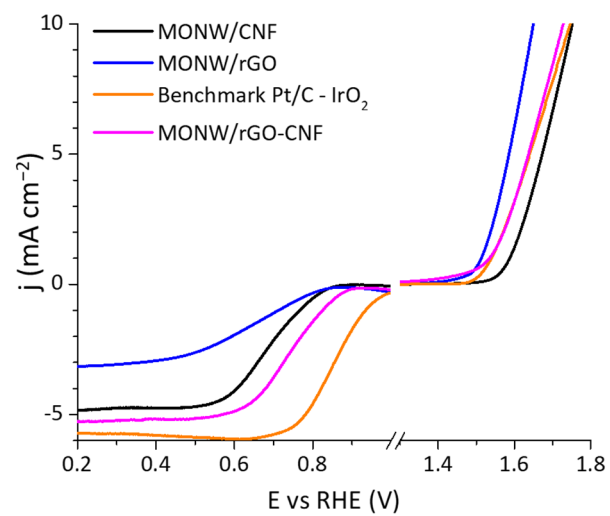


Figure 8. ORR and OER LSVs of selected catalysts. Experiments carried out in a RDE at 1600 rpm.

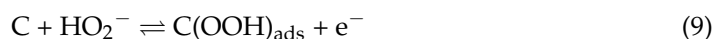
Table 4. Electrocatalytic parameters obtained for rGO-CNF, MONW/rGO-CNF, the benchmark catalysts, and similar catalysts from literature.

Catalyst	Oxygen Reduction Reaction				Oxygen Evolution Reaction		Reversibility ORR/OER	Ref.
	$E_{\text{ORR, onset}}^{\dagger}$ (V vs. RHE)	j_d @ 1600 rpm (mA cm^{-2})	$E_{1/2}$ (V vs. RHE)	n	$E_{\text{OER, onset}}^{\dagger}$ (V vs. RHE)	E_{10} (V vs. RHE)	ΔE (V)	
rGO-CNF	0.79	−3.80	0.69	2.9	1.58	1.76	1.07	This work
MONW/rGO-CNF	0.90	−5.26	0.74	3.7	1.54	1.73	0.99	This work
Pt/C-IrO ₂	1.02	−5.72	0.85	4	1.53	1.75	-	This work
MnO _x /CNTs	0.85 *	−4.90	0.77 *	3.6	1.58 *	0.91 *	0.91 *	[25]
MnO ₂ -C(ultrathin amorphous)	0.97	−5.81	0.81	4	1.45	1.59	0.78	[56]
α -MnO ₂ (cryptomelane)/Vulcan	0.88 *	−4.1	0.79 *	4	1.58 *	1.73 *	0.94 *	[57]
Mn-MOF @rGO	1.09 *	−2.03	0.98 *	-	1.75 *	1.84 *	0.86 *	[58]
Mn _x O _y /N-carbon	0.85	−5.0	0.77	-	1.61	1.68	0.91	[59]
MnO _x /S-carbon	0.94	−4.5	0.81	3.7	1.33 *	1.62 *	0.81 *	[60]

* IR corrected. - Not reported or not relevant. † Onset potentials for OER and ORR according to the definitions of this work.

Table 4 also compares our catalyst with some similar materials based on manganese and carbon found in the literature. It is possible to see that our catalyst MONW/rGO-CNF has an interesting activity. Some materials, like those in [25,57,58], show reversibility gaps up to 0.13 V lower, but these differences must be considered with caution, as their results are reported corrected by IR, unlike in this work. It is interesting to note that the material by He et al. [25] has a relatively high activity, even though it uses carbon nanotubes, suggesting that the CNT used in this study have low activity due to their high number of layers and low surface area, rather than the cause being the structure of CNT. The work by Wahab et al. [58], uses reduced graphene oxide and contrary to our findings, their material has an extraordinary activity for ORR, but lower activity than our MONW/rGO-CNF material. The referenced work uses a metal-organic framework (MOF) with manganese supported over reduced graphene oxide, which may result in different interactions between the carbon and metallic phases. Moreover, the MOF as a catalyst with rGO showed extremely limited activity towards ORR, which reinforces our idea that it is a combination of graphitic carbon phases and manganese phases responsible for the high activity of the catalysts rather than the carbon phase just working as a conductive additive.

The good ORR activity of the composite reveals a synergistic effect that must comprise the three phases: the two carbons and the manganese oxide, which can be derived from the analysis of the separated phases (see Figure S6d). As stated before, oxygen reduction on rGO involves the transfer of 2.9 electrons, indicating partial reduction to peroxide. However, some works have shown that peroxy can adsorb over the edges of graphene layers [38]. Therefore, and most probably, the superior number of electrons exchanged in MONW/rGO-CNF is explained by a 2+2 mechanism. We propose that the reduction of hydroperoxide (Equation (9)) can take place between two adsorbed species (Equations (9) and (10)).



In this case, the hydroxyperoxide anion electrochemically adsorbs over a carbon edge site, either on rGO or CNF. It is crucial for this mechanism to take place to ensure good contact between carbon and manganese phases. A possible explanation for the superior performance of MOWN/rGO-CNF over that of the rest of the carbon composites is that graphene oxide provides a large surface area where peroxy can adsorb, and CNF improves the contact between the carbon and manganese phases. In this regard, Poux et al. [23] synthesized composites containing La-Sr-Mn perovskites and pyrolytic carbon and reached the conclusion that carbon enhances the activity of the perovskites in two different ways: first, it improves the electrical conductivity from the current collector to the outside layers

of the perovskite, and second, it provides a large area where oxygen can adsorb and begin to reduce. Despite these two effects are definitively important, they are not enough by themselves to explain the increase in electrons exchanged during ORR. Our proposed explanation can deal with this observation.

Even though composite MONW/rGO-CNF has a slightly lower activity for OER than MONW/rGO, especially at high current densities, it holds especially well against the benchmark catalyst, IrO₂. They have an almost identical onset potential, but the composite has a 20 mV lower E₁₀, which may be a consequence of the good conductivity of carbon materials in comparison to metallic oxides. Therefore, composite MONW/rGO-CNF has a good compromise in activity towards ORR and OER, and consequently, it exhibits the lowest value of reversibility gap amongst the tested catalysts, with 0.99 V (see Table 3).

The activity of the MONW/rGO-CNF hybrid catalyst was also assessed, analyzing Tafel slopes for both ORR and OER, compared to the benchmark catalysts, as shown in Figure 9 and Table 5.

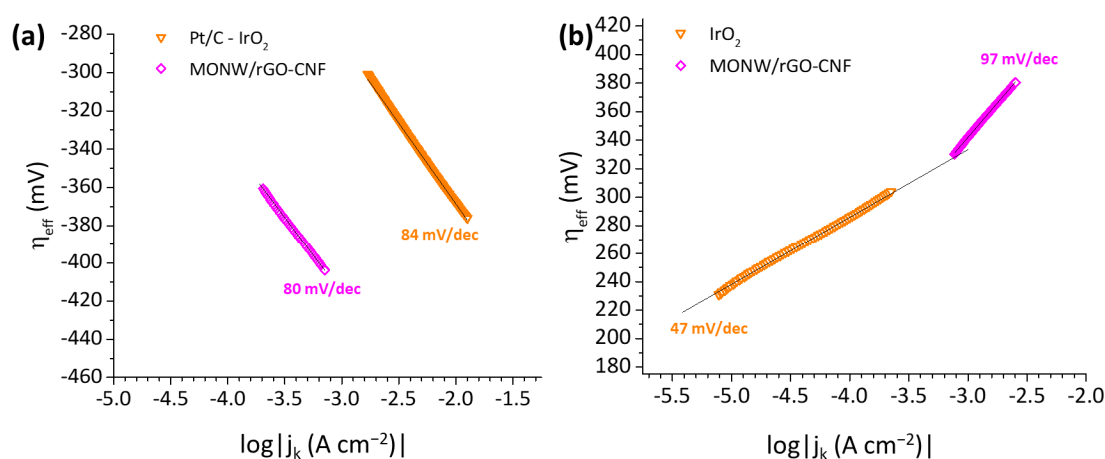


Figure 9. ORR (a) and OER (b) Tafel plots of hybrid MONW/rGO-CNF composite and benchmark catalysts.

Table 5. Kinetic parameters obtained from the Tafel slopes for rGO-CNF, MONW/rGO-CNF and benchmark catalysts.

Catalyst	Oxygen Reduction Reaction		Oxygen Evolution Reaction	
	j_0 (mA cm ⁻²)	Tafel Slope (mV dec ⁻¹)	j_0 (mA cm ⁻²)	Tafel Slope (mV dec ⁻¹)
rGO-CNF	2.6×10^{-12}	42	4.6×10^{-4}	98
MONW/rGO-CNF	6.3×10^{-6}	80	2.9×10^{-6}	97
Pt/C-IrO ₂	4.2×10^{-4}	84	1.0×10^{-7}	47

Tafel slopes for ORR also reveal the superior behavior of the benchmark catalyst. Even though it is not the catalyst with the lowest slope, it has a superior exchange current density (j_0), as is evident from the position of the data in the graph. Pt/C has a j_0 of 4.2×10^{-4} mA cm⁻², two orders of magnitude higher than the MONW/rGO-CNF composite, 6.3×10^{-6} mA cm⁻², which has a comparable Tafel slope. None of our carbon-manganese catalysts can match the high activity of the well-dispersed, high surface-area Pt/C catalyst towards ORR. In the case of the OER, the benchmark material has the lowest Tafel slope (half that of MONW/rGO-CNF); however, composite MONW/rGO (Figure 6) has a higher j_0 , explaining its better activity. Although the ORR activity of the MONW/rGO-CNF is significantly lower than that of Pt/C, its good performance (bifunctionality) for both ORR and OER makes it an interesting choice due to the lower cost and abundance of manganese compared to Pt.

The low ORR Tafel slope of hybrid carbon rGO-CNF of only 42 mV dec^{-1} (Figure S10a) is indicative that, in this material, the second electron transfer limits the kinetics of the reaction. In this case, it is possible to see that the different phases have the ability to catalyze the different steps of the reaction and yield the most active of the synthesized catalysts.

The hypothesis of different phases catalyzing different steps of the reaction was studied through EIS (Figure 10). Figure 10a shows the Nyquist plot for ORR for MONW. A large transfer resistance can be observed over a single semicircle. The equivalent circuit is visible inside the plot. By contrast, the Nyquist plot of ORR for the MONW/rGO-CNF catalyst can be modeled by a series of two RQ elements (resistance in parallel with a constant phase element). Despite the presence of two resistances, their lower values result in a lower total charge transfer resistance, in agreement with the higher activity observed for this catalyst. More interestingly, the presence of a series of two RQ elements suggests the transfer of two electrons or, at least, two processes with similar rates, indicating that there is no single rate-determining step for ORR for this catalyst, contrary to what happens in the MONW catalyst. The large difference in the admittance of the constant phase elements in the circuit in Figure 10b suggests that the two different electron transfers could take place over different surfaces, in agreement with our hypothesis.

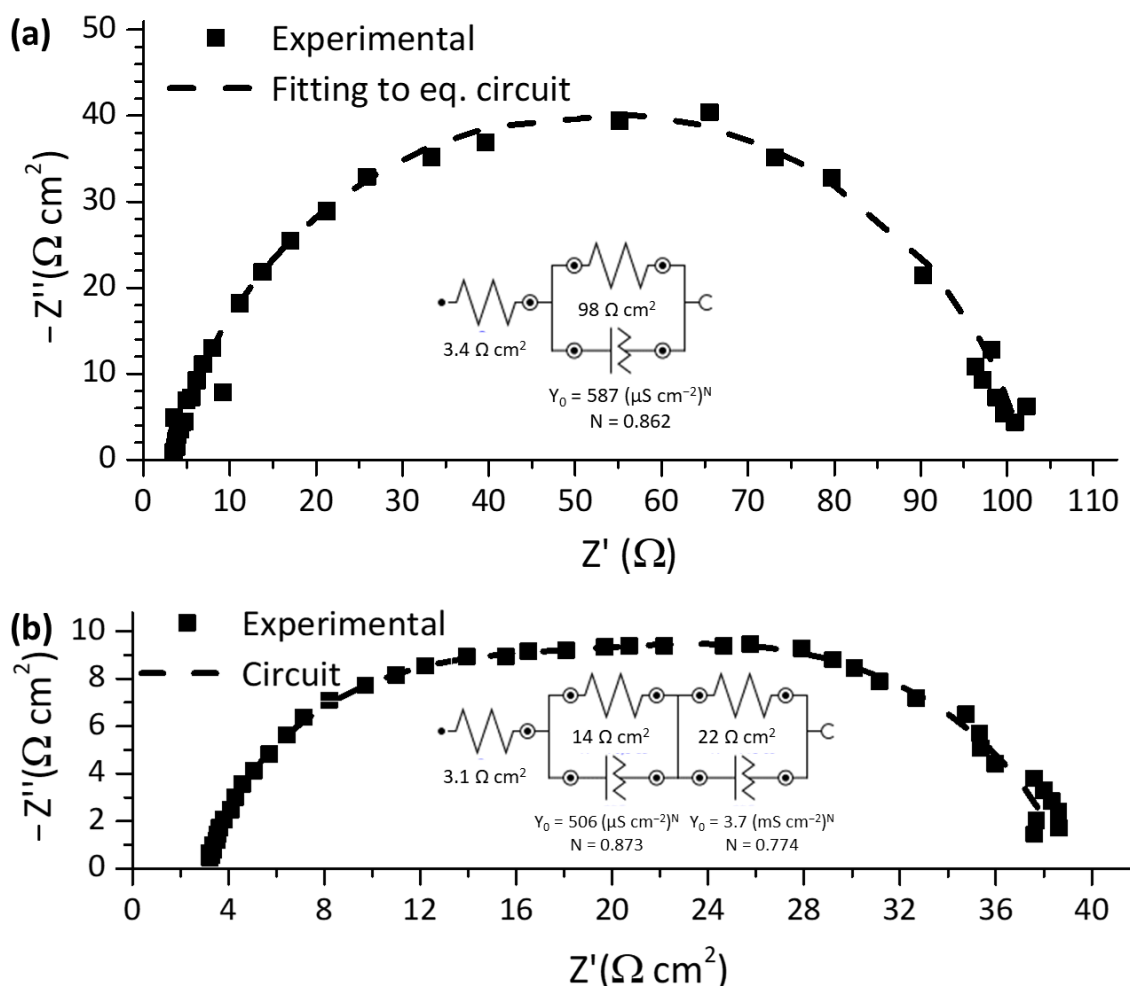


Figure 10. Nyquist diagrams for ORR, EIS tests at $E_j = 1$ for: (a) MONW; and (b) MONW/rGO-CNF.

2.4. Stability Studies

The durability and resistance to degradation of the MONW/CNF, MONW/rGO and MONW/rGO-CNF catalysts were assessed in an endurance test at $\pm 10 \text{ mA cm}^{-2}$ for 20 h in a gas-diffusion electrode in 6 M KOH (Figure 11). Catalyst MONW/rGO-CNF

shows remarkable stability, with the potential for OER increasing an average of 1.9 mV per hour of operation and the overpotential for ORR increasing less than 1 mV per hour. The overpotential for ORR (corrected by the ohmic potential loss, which was obtained from electrochemical impedance spectroscopy, see Figure S13) is around 450 mV and for OER, ca. 330 mV in the first cycle, resulting in a potential gap between ORR and OER at 10 mA cm^{-2} (IR free) of ca. 780 mV. This is consistent with what was observed during the LSVs (Table 3), as the observed onset potential for OER was lower than for ORR in those conditions. The stability of the catalyst towards OER is especially remarkable since it is considerably better than the benchmark IrO_2 catalyst. Gebreslase et al. [61] showed that after only 5 h of operation at 10 mA cm^{-2} in 1 M KOH, the IrO_2 catalyst began to quickly lose activity.

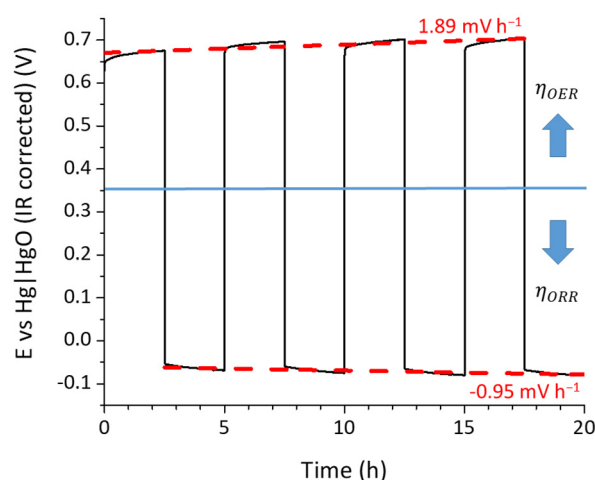


Figure 11. Endurance test carried out over a GDE with catalyst MONW/rGO-CNF in 6 M KOH. Potentials corrected for IR.

Figure S12 (Section S2.6 in Supporting Information) shows the endurance test for MONW/CNF and MONW/rGO, alongside the comparison with MONW/rGO-CNF. Catalyst MONW/CNF is also significantly stable, showing an increase in overpotential of 1.8 mV h^{-1} for ORR and 4.2 mV h^{-1} for OER, but exhibits a wider gap between the potentials for OER and ORR. Catalyst MONW/rGO has a good performance at the beginning, especially for OER, but quickly starts to deactivate, incrementing its overpotential at a rate of 2.1 mV h^{-1} for ORR and 11.3 mV h^{-1} for OER. By the end of the 20 h, the difference of potentials in this catalyst is almost 1100 mV.

3. Materials and Methods

3.1. Catalysts Synthesis

Manganese oxide nanowires (MONW) were synthesized following a procedure described elsewhere [24]. Briefly, 100 mL of an aqueous solution with 1.26 g of potassium permanganate (99%, Sigma-Aldrich, St. Louis, MO, USA) and 2.8 mL of concentrated hydrochloric acid (37% wt., Fluka) was stirred at room temperature for 30 min and then transferred to an autoclave at $120 \text{ }^\circ\text{C}$ for 12 h. A brown precipitate formed, which was washed with 2 L of deionized water (DI) and dried overnight at $70 \text{ }^\circ\text{C}$.

Carbon nanofibers (CNF) and nanotubes (CNT) were obtained by catalytic decomposition of methane, varying the synthesis catalyst and temperature. The catalyst for CNF was based on $\text{NiCuAl}_2\text{O}_3$, as described by Sebastián et al. [62], and for CNT, Fe_2O_3 nanoparticles (<50 nm) obtained from Sigma-Aldrich. The catalysts were reduced with a 10 mL min^{-1} flow of hydrogen at $550 \text{ }^\circ\text{C}$ for CNF and at $700 \text{ }^\circ\text{C}$ for CNT. Subsequently, the temperature was raised under a flow of nitrogen up to $700 \text{ }^\circ\text{C}$ for CNF and $900 \text{ }^\circ\text{C}$ for CNT, after which a flow of 50 mL min^{-1} of methane was passed through the reactor for 3 h.

Reduced graphene oxide was synthesized by the Tour's method [63]. Briefly, 120 mL of concentrated sulphuric acid (98% Labkem) and 13.3 mL of phosphoric acid (85% Panreac) were mixed in a flask. After cooling, 1 g of graphite (Sigma-Aldrich) was added to the mixture under stirring. An amount of 6 g of KMnO_4 (99%, Sigma-Aldrich) was added slowly under stirring. The flask was then kept at 50 °C under stirring for 18 h. After that period, the mixture was poured over 135 mL of DI water ice, obtaining a brownish solution that was stirred for 30 min at 95 °C and then left to cool to room temperature. A solution of H_2O_2 (30% wt., 8 mL) was poured drop by drop, and then the mixture was placed in an ultrasound bath for 30 min to exfoliate the graphite oxide layers. Finally, the graphene oxide (GO) dispersion was washed and centrifuged repeatedly until a neutral pH was achieved, and the collected solid was dried overnight at 65 °C. The graphene oxide was reduced at 800 °C in a nitrogen atmosphere for 2 h to obtain reduced graphene oxide (rGO).

The carbon materials and MONW were mixed in a planetary ball mill in a 1:1 mass ratio, with a rotation speed of 100 rpm and using ethanol as a dispersing agent. The obtained composites were named MONW/C, where C is CNF, CNT or rGO.

A hybrid carbon material (rGO-CNF) was also synthesized by growing nanofibers in reduced graphene oxide. To do this, 0.7 g of GO was dispersed in 140 mL of water, and a solution of 1.48 g of $\text{Ni}(\text{NO}_3)_2 \cdot 6\text{H}_2\text{O}$ in 68 mL of water was added dropwise. The pH of the mixture was then raised to 5 with NaOH, and a solution with 0.38 g of NaBH_4 in 204 mL of water was slowly added. The solid was then filtered, washed with abundant water and dried overnight at 60 °C. This Ni oxide on GO material was introduced in a tubular quartz reactor, reduced in H_2 at 550 °C for one hour and then CH_4 was passed at 700 °C for one hour for the growth of CNF by catalytic decomposition on Ni particles.

3.2. Physical-Chemical Characterization

MONW and carbon materials were characterized using solid-state characterization techniques. The crystalline structures of the materials were investigated using powder X-Ray Diffraction (XRD). The equipment used was a Bruker AXS D8 Advance diffractometer (Billerica, MA, USA), which has a Cu $\text{K}\alpha$ radiation source and a θ - θ configuration. The interplanar distances were obtained using Bragg's equation, and the number of graphitic planes was obtained by dividing the 002 crystal size (obtained from Scherrer's equation) by the interplanar distance. The determination of the crystallographic phases was carried out through Rietveld refinement. The morphology of MONW and carbon nanostructures was investigated by both transmission (TEM) and scanning (SEM) electron microscopy. TEM images were acquired with a Tecnai F30 microscope (ThermoFisher, Waltham, Massachusetts, Estados Unidos) operated at 300 kV. The samples were ultrasonically dispersed in ethanol for 15 min and then placed in a Cu carbon grid. SEM images were obtained with a Hitachi 3400-N microscope (Hitachi Ltd., Tokyo, Japan) with the powdered samples directly placed on a carbon tape. Textural features of MONW were assessed through nitrogen physisorption at -196 °C in Micromeritics ASAP 2020 (Norcross, GA, USA). The amount of metals in the samples was determined by inductively coupled plasma combined with atomic emission spectrometry (ICP-AES) using an Xpctroblue-EOP-TI FMT26 spectrometer (SPECTRO Analytical Instruments, Kleve, Germany). In addition, the carbon and hydrogen content of carbon materials was determined by elemental analysis (EA) in a Thermo Flash 1112 analyzer (ThermoScientific, Waltham, MA, USA).

3.3. Electrochemical Characterization

All the electrochemical tests were carried out in a three-electrode cell connected to an Autolab potentiostat/galvanostat (Metrohm 302N, Metrohm Hispania, Madrid, Spain). The activity of the electrocatalysts was assessed through linear sweep voltammeteries (LSVs) in a 0.1 M KOH electrolyte, using a reversible hydrogen electrode as the reference electrode and a graphite rod as the counter electrode. The working electrode was a glassy carbon rotating disk electrode (RDE, 5 mm diameter), on top of which a fine layer of the catalyst was deposited. To do so, an ink was prepared dispersing 5 mg of the catalyst and 10 μL of

Nafion (10% wt., Sigma-Aldrich, St. Louis, MO, USA) in 490 μL of ethanol under sonication and then deposited over the RDE in order to achieve a loading of 1 mg cm^{-2} . The LSVs to evaluate the ORR were performed in the range 1.2–0.2 V vs. RHE at a sweeping rate of 5 mV s^{-1} in oxygen-saturated electrolyte and at different rotation speeds (400, 625, 900, 1600 and 2500 rpm). Prior to the ORR LSVs, blank LSVs in nitrogen-saturated electrolyte were complete in the same potential range and used as a baseline. OER tests were carried out at 1600 rpm in the 1.1–1.8 V vs. RHE potential range at 5 mV s^{-1} of scan rate. Electrochemical impedance spectroscopy (EIS) tests were executed at the potential at which current had a magnitude of 1 mA cm^{-2} for both ORR ($E_j = 1$) and OER, with a sine wave of 10 mV of amplitude and in the range between 10 kHz and 100 mHz, acquiring ten points per decade. Endurance tests were carried out over a gas diffusion electrode of 0.5 cm^2 of exposed area in the strong basic electrolyte (6 M KOH). An ink of the same characteristics as the one of the RDE was sprayed over carbon paper, achieving a coverage of ca. $800 \mu\text{g cm}^{-2}$. The reference electrode was a Hg|HgO electrode in 1 M KOH. Consecutive cycles (OER/ORR) of 2.5 h for each reaction at a current density of $\pm 10 \text{ mA cm}^{-2}$ were run.

4. Conclusions

Three different carbon nanostructures (carbon nanofibers, carbon nanotubes and reduced graphene oxide) were synthesized and mixed with manganese oxide nanowires to obtain bifunctional oxygen electrocatalysts. The type of carbon employed in the catalyst had an important effect on the activity, being the catalyst synthesized with CNF the most active towards ORR and the catalyst with rGO the most active towards OER, even surpassing the performance of the benchmark IrO_2 catalyst. Catalysts with CNT showed poor activity for both reactions, which was ascribed to their low surface area and lack of structural defects. The Koutecky–Levich plots show that the MONW/C catalysts have an increased number of electrons transferred in comparison to the phases on their own, indicating a synergistic effect that goes beyond just increasing conductivity or enhancing surface area but also changes the pathway of the reaction. The analysis of Tafel plots and electrochemical impedance spectroscopy allowed us to conclude that carbon and manganese oxide phases can catalyze different steps of the reaction pathways, and thus, by mixing them, a catalyst with lower energetic barriers for the reactions could be obtained. With this information in mind, we synthesized a hybrid rGO-CNF material and mixed it with MONW, which showed increased activity towards ORR in comparison to MONW/CNF and a closer activity towards OER than that of catalyst MONW/rGO. The hybrid MONW/rGO-CNF catalyst was tested in demanding conditions in a gas diffusion electrode (6 M KOH, at $\pm 10 \text{ mA cm}^{-2}$) and showed remarkable stability for 20 h of operation, maintaining less than 0.77 V of difference between the potentials for OER and ORR (IR corrected) under the mentioned conditions. This work proves that the structure of carbon materials used as an additive in manganese bifunctional oxygen catalysts plays a key role in both the mechanisms of the reactions and the performance of the catalysts and that this can be exploited to rationally design catalysts with enhanced activity and/or bifunctionality.

Supplementary Materials: The following supporting information can be downloaded at <https://www.mdpi.com/article/10.3390/catal13091240/s1>. S1. Additional physical-chemical characterization of manganese oxide nanowires; S1.1. Morphology; Figure S1. (a) TEM and (b) SEM micrographs for MONW; S1.2. X-Ray diffraction; Figure S2. Diffractogram of MONW; S1.3. X-ray photoelectron spectroscopy; Figure S3. XPS spectra of orbitals: (a) Mn2p and (b) O1s of MONW; S1.4. Nitrogen physisorption; Figure S4. (a) Nitrogen physisorption for MONW at 96 K and, (b) Pore size distribution (BJH desorption); S2. Additional electrochemical characterization of manganese oxide nanowire–carbon composites; S2.1 Effect of acid-leaching on carbon nanotubes; Figure S5. Comparison between the catalytic activities of pristine carbon nanotubes and acid-leached carbon nanotubes (CNT-AL); S2.2. Comparison between the single materials and the composite catalysts; Figure S6. Comparison between the catalytic activities of carbon materials and their composites: (a) CNF, (b) CNT, (c) rGO and, (d) rGO-CNF; S2.3. Koutecky–Levich plots; Table S1. Parameters and properties of the electrochemical system used in the Levich equation; Figure S7. LSVs at 400, 625, 900, 1600 rpm

rotation speed of materials: (a) CNF, (b) CNT, (c) rGO and, (d) MONW; Figure S8. LSVs at 400, 625, 900, 1600 rpm rotation speed of materials: (a) MONW/CNF, (b) MONW/CNT and, (c) MONW/rGO; Figure S9. Koutecky–Levich plots at $E = 0.4$ V vs. RHE of carbon materials and manganese oxide; S2.4. Tafel plots; S2.5. Electrochemical characterization of composite MONW/mm[rGO-CNF]; Figure S11. Comparative performance of composite MONW/mm[rGO-CNF] with respect to MONW/C catalysts; S2.6. Durability tests; Figure S12. Endurance test carried out over a GDE with catalysts (a) MONW/CNF and (b) MONW/rGO in 6M KOH. Potentials corrected for IR; Figure S13. Nyquist diagrams (top: ORR, bottom: OER) for EIS tests for MONW/CNF-rGO.

Author Contributions: Conceptualization, N.I.V.-M., C.A. and D.S.; methodology, N.I.V.-M., C.A. and D.S.; validation, N.I.V.-M. and N.O.; formal analysis, N.I.V.-M., C.A. and D.S.; investigation, N.I.V.-M., C.A., D.S. and N.O.; resources, C.A. and M.J.L.; data curation, N.I.V.-M. and N.O.; writing—original draft preparation, N.I.V.-M.; writing—review and editing, C.A. and D.S.; visualization, N.I.V.-M. and N.O.; supervision, C.A. and M.J.L.; project administration, C.A., D.S. and M.J.L.; funding acquisition, C.A., D.S. and M.J.L. All authors have read and agreed to the published version of the manuscript.

Funding: The authors wish to acknowledge Ministerio de Ciencia e Innovación and Agencia Estatal de Investigación (MCIN/AEI/10.13039/501100011033) for the PID2020-115848RB-C21 grant. The authors also thank the European Union and the NextGeneration EU program for the funding of grant TED2021-130279A-I00. The authors also acknowledge Gobierno de Aragón (DGA) for the financial support to Grupo de Conversión de Combustibles (T06_20R). N. Villanueva also acknowledges DGA for his pre-doctoral contract. The authors would like to acknowledge the use of the Servicio General de Apoyo a la Investigación-SAI, Universidad de Zaragoza.

Data Availability Statement: The data presented in this study are available on request from the corresponding author.

Conflicts of Interest: The authors declare no conflict of interest.

References

1. McKerracher, R.D.; Ponce de Leon, C.; Wills, R.G.A.; Shah, A.A.; Walsh, F.C. A Review of the Iron-Air Secondary Battery for Energy Storage. *Chempluschem* **2015**, *80*, 323–335. [[CrossRef](#)]
2. Wang, Y.; Leung, D.Y.C.; Xuan, J.; Wang, H. A review on unitized regenerative fuel cell technologies, part B: Unitized regenerative alkaline fuel cell, solid oxide fuel cell, and microfluidic fuel cell. *Renew. Sustain. Energy Rev.* **2017**, *75*, 775–795. [[CrossRef](#)]
3. Xie, X.; Du, L.; Yan, L.; Park, S.; Qiu, Y.; Sokolowski, J.; Wang, W.; Shao, Y. Oxygen Evolution Reaction in Alkaline Environment: Material Challenges and Solutions. *Adv. Funct. Mater.* **2022**, *32*, 2110036. [[CrossRef](#)]
4. Shao, Y.; Jiang, Z.; Zhang, Q.; Guan, J. Progress in Nonmetal-Doped Graphene Electrocatalysts for the Oxygen Reduction Reaction. *ChemSusChem* **2019**, *12*, 2133–2146. [[CrossRef](#)] [[PubMed](#)]
5. Yang, C.J. An impending platinum crisis and its implications for the future of the automobile. *Energy Policy* **2009**, *37*, 1805–1808. [[CrossRef](#)]
6. Minke, C.; Suermann, M.; Bensmann, B.; Hanke-Rauschenbach, R. Is iridium demand a potential bottleneck in the realization of large-scale PEM water electrolysis? *Int. J. Hydrog. Energy* **2021**, *46*, 23581–23590. [[CrossRef](#)]
7. Alegre, C.; Stassi, A.; Modica, E.; Lo Vecchio, C.; Aricò, A.S.; Baglio, V. Investigation of the activity and stability of Pd-based catalysts towards the oxygen reduction (ORR) and evolution reactions (OER) in iron-air batteries. *RSC Adv.* **2015**, *5*, 25424–25427. [[CrossRef](#)]
8. McKerracher, R.D.; Alegre, C.; Baglio, V.; Aricò, A.S.; Ponce De León, C.; Mornaghini, F.; Rodlert, M.; Walsh, F.C. A nanostructured bifunctional Pd/C gas-diffusion electrode for metal-air batteries. *Electrochim. Acta* **2015**, *174*, 508–515. [[CrossRef](#)]
9. Alegre, C.; Modica, E.; Lo Vecchio, C.; Sebastián, D.; Lázaro, M.J.; Aricò, A.S.; Baglio, V. Carbon Nanofibers as Advanced Pd Catalyst Supports for the Air Electrode of Alkaline Metal-Air Batteries. *Chempluschem* **2015**, *80*, 1384–1388. [[CrossRef](#)]
10. Zhao, Q.; Yan, Z.; Chen, C.; Chen, J. Spinels: Controlled Preparation, Oxygen Reduction/Evolution Reaction Application, and beyond. *Chem. Rev.* **2017**, *117*, 10121–10211. [[CrossRef](#)]
11. Alegre, C.; Modica, E.; Aricò, A.S.; Baglio, V. Bifunctional oxygen electrode based on a perovskite/carbon composite for electrochemical devices. *J. Electroanal. Chem.* **2018**, *808*, 412–419. [[CrossRef](#)]
12. Rashkova, V.; Kitova, S.; Konstantinov, I.; Vitanov, T. Vacuum evaporated thin films of mixed cobalt and nickel oxides as electrocatalyst for oxygen evolution and reduction. *Electrochim. Acta* **2002**, *47*, 1555–1560. [[CrossRef](#)]
13. Indra, A.; Menezes, P.W.; Sahraie, N.R.; Bergmann, A.; Das, C.; Tallarida, M.; Schmeißer, D.; Strasser, P.; Driess, M. Unification of catalytic water oxidation and oxygen reduction reactions: Amorphous beat crystalline cobalt iron oxides. *J. Am. Chem. Soc.* **2014**, *136*, 17530–17536. [[CrossRef](#)]
14. Hazarika, K.K.; Goswami, C.; Saikia, H.; Borah, B.J.; Bharali, P. Cubic Mn₂O₃ nanoparticles on carbon as bifunctional electrocatalyst for oxygen reduction and oxygen evolution reactions. *Mol. Catal.* **2018**, *451*, 153–160. [[CrossRef](#)]

15. Wang, Y.; Yang, D.; Li, S.; Zhang, L.; Zheng, G.; Guo, L. Layered copper manganese oxide for the efficient catalytic CO and VOCs oxidation. *Chem. Eng. J.* **2019**, *357*, 258–268. [[CrossRef](#)]
16. Yang, S.; Wang, Z.; Cao, Z.; Mao, X.; Shi, M.; Li, Y.; Zhang, R.; Yin, Y. Facile synthesis of well dispersed spinel cobalt manganese oxides microsphere as efficient bi-functional electrocatalysts for oxygen reduction reaction and oxygen evolution reaction. *J. Alloys Compd.* **2017**, *721*, 482–491. [[CrossRef](#)]
17. Gu, Y.; Yan, G.; Lian, Y.; Qi, P.; Mu, Q.; Zhang, C.; Deng, Z.; Peng, Y. MnIII-enriched α -MnO₂ nanowires as efficient bifunctional oxygen catalysts for rechargeable Zn-air batteries. *Energy Storage Mater.* **2019**, *23*, 252–260. [[CrossRef](#)]
18. Chatenet, M.; Pollet, B.G.; Dekel, D.R.; Dionigi, F.; Deseure, J.; Millet, P.; Braatz, R.D.; Bazant, M.Z.; Eikerling, M.; Staffell, I.; et al. Water electrolysis: From textbook knowledge to the latest scientific strategies and industrial developments. *Chem. Soc. Rev.* **2022**, *51*, 4583–4762. [[CrossRef](#)]
19. Jiang, J.; Li, Y.; Liu, J.; Huang, X.; Yuan, C.; Lou, X.W. Recent advances in metal oxide-based electrode architecture design for electrochemical energy storage. *Adv. Mater.* **2012**, *24*, 5166–5180. [[CrossRef](#)]
20. Fu, G.; Yan, X.; Chen, Y.; Xu, L.; Sun, D.; Lee, J.M.; Tang, Y. Boosting Bifunctional Oxygen Electrocatalysis with 3D Graphene Aerogel-Supported Ni/MnO Particles. *Adv. Mater.* **2018**, *30*, 1704609. [[CrossRef](#)]
21. Xu, N.; Zhang, Y.; Wang, M.; Fan, X.; Zhang, T.; Peng, L.; Zhou, X.D.; Qiao, J. High-performing rechargeable/flexible zinc-air batteries by coordinated hierarchical Bi-metallic electrocatalyst and heterostructure anion exchange membrane. *Nano Energy* **2019**, *65*, 104021. [[CrossRef](#)]
22. Xiang, W.; Zhao, Y.; Jiang, Z.; Li, X.; Zhang, H.; Sun, Y.; Ning, Z.; Du, F.; Gao, P.; Qian, J.; et al. Palladium single atoms supported by interwoven carbon nanotube and manganese oxide nanowire networks for enhanced electrocatalysis. *J. Mater. Chem. A* **2018**, *6*, 23366–23377. [[CrossRef](#)]
23. Poux, T.; Napolskiy, F.S.; Dintzer, T.; Kéranguéven, G.; Istomin, S.Y.; Tsirlina, G.A.; Antipov, E.V.; Savinova, E.R. Dual role of carbon in the catalytic layers of perovskite/carbon composites for the electrocatalytic oxygen reduction reaction. *Catal. Today* **2012**, *189*, 83–92. [[CrossRef](#)]
24. Villanueva-Martínez, N.I.; Alegre, C.; Martínez-Visús, I.; Lázaro, M.J. Bifunctional oxygen electrocatalysts based on non-critical raw materials: Carbon nanostructures and iron-doped manganese oxide nanowires. *Catal. Today* **2023**, *420*, 114083. [[CrossRef](#)]
25. He, M.; Jin, X.; Chen, F.; Chen, J.; Min, J.; Duan, H.; Kuang, X.; Li, J.; Wu, Z.; Li, J. Synergistic effect of Mn³⁺ and oxygen vacancy on the bifunctional oxygen electrocatalytic performance of MnOX/CNTs composites. *J. Alloys Compd.* **2023**, *933*, 167728. [[CrossRef](#)]
26. Niu, Y.; Teng, X.; Gong, S.; Liu, X.; Xu, M.; Chen, Z. Boosting oxygen electrocatalysis for flexible zinc-air batteries by interfacing iron group metals and manganese oxide in porous carbon nanowires. *Energy Storage Mater.* **2021**, *43*, 42–52. [[CrossRef](#)]
27. Cuong, T.V.; Pham, V.H.; Tran, Q.T.; Chung, J.S.; Shin, E.W.; Kim, J.S.; Kim, E.J. Optoelectronic properties of graphene thin films prepared by thermal reduction of graphene oxide. *Mater. Lett.* **2010**, *64*, 765–767. [[CrossRef](#)]
28. Liu, T.H.; Gajewski, G.; Pao, C.W.; Chang, C.C. Structure, energy, and structural transformations of graphene grain boundaries from atomistic simulations. *Carbon N. Y.* **2011**, *49*, 2306–2317. [[CrossRef](#)]
29. Krishnamoorthy, K.; Veerapandian, M.; Yun, K.; Kim, S.J. The chemical and structural analysis of graphene oxide with different degrees of oxidation. *Carbon N. Y.* **2013**, *53*, 38–49. [[CrossRef](#)]
30. Stobinski, L.; Lesiak, B.; Malolepszy, A.; Mazurkiewicz, M.; Mierzwa, B.; Zemek, J.; Jiricek, P.; Bieloshapka, I. Graphene oxide and reduced graphene oxide studied by the XRD, TEM and electron spectroscopy methods. *J. Electron Spectros. Relat. Phenomena* **2014**, *195*, 145–154. [[CrossRef](#)]
31. Paulchamy, B.; Arthi, G.; Lignesh, B.D. A Simple Approach to Stepwise Synthesis of Graphene Oxide Nanomaterial. *J. Nanomed. Nanotechnol.* **2015**, *6*, 1000253. [[CrossRef](#)]
32. Shen, J.; Hu, Y.; Shi, M.; Lu, X.; Qin, C.; Li, C.; Ye, M. Fast and facile preparation of graphene oxide and reduced graphene oxide nanoplatelets. *Chem. Mater.* **2009**, *21*, 3514–3520. [[CrossRef](#)]
33. Saleem, H.; Haneef, M.; Abbasi, H.Y. Synthesis route of reduced graphene oxide via thermal reduction of chemically exfoliated graphene oxide. *Mater. Chem. Phys.* **2018**, *204*, 1–7. [[CrossRef](#)]
34. Tientong, J.; Garcia, S.; Thurber, C.R.; Golden, T.D. Synthesis of nickel and nickel hydroxide nanopowders by simplified chemical reduction. *J. Nanotechnol.* **2014**, *2014*, 193162. [[CrossRef](#)]
35. Hosseynizadeh Khezri, S.; Yazdani, A.; Khordad, R. Pure iron nanoparticles prepared by electric arc discharge method in ethylene glycol. *EPJ Appl. Phys.* **2012**, *59*, 30401. [[CrossRef](#)]
36. Lu, X.; Qin, Z.; Zhang, Y.; Wang, X.; Li, F.; Ding, B.; Hu, Z. Study of the paramagnetic-antiferromagnetic transition and the $\gamma \rightarrow \epsilon$ martensitic transformation in Fe-Mn alloys. *J. Mater. Sci.* **2000**, *35*, 5597–5603. [[CrossRef](#)]
37. Mathur, A.; Halder, A. One-step synthesis of bifunctional iron-doped manganese oxide nanorods for rechargeable zinc-air batteries. *Catal. Sci. Technol.* **2019**, *9*, 1245–1254. [[CrossRef](#)]
38. Shen, Y.; Zhu, Y.; Sunarso, J.; Guan, D.; Liu, B.; Liu, H.; Zhou, W.; Shao, Z. New Phosphorus-Doped Perovskite Oxide as an Oxygen Reduction Reaction Electrocatalyst in an Alkaline Solution. *Chem. A Eur. J.* **2018**, *24*, 6950–6957. [[CrossRef](#)]
39. Briggs, D. Handbook of X-ray Photoelectron Spectroscopy C. D. Wanger, W.M. Riggs, L.E. Davis, J.F. Moulder and G. E. Muilenberg Perkin-Elmer Corp., Physical Electronics Division, Eden Prairie, Minnesota, USA, 1979. 190 pp. \$195. *Surf. Interface Anal.* **1981**, *3*, v. [[CrossRef](#)]
40. Santos, V.P.; Pereira, M.F.R.; Órfão, J.J.M.; Figueiredo, J.L. The role of lattice oxygen on the activity of manganese oxides towards the oxidation of volatile organic compounds. *Appl. Catal. B Environ.* **2010**, *99*, 353–363. [[CrossRef](#)]

41. Kabalan, I.; Lebeau, B.; Fadlallah, M.B.; Toufaily, J.; Hamieh, T.; Bellat, J.P.; Daou, T.J. Hierarchical faujasite-type zeolite for molecular decontamination. *J. Nanosci. Nanotechnol.* **2016**, *16*, 9318–9322. [[CrossRef](#)]
42. Waki, K.; Wong, R.A.; Oktaviano, H.S.; Fujio, T.; Nagai, T.; Kimoto, K.; Yamada, K. Non-nitrogen doped and non-metal oxygen reduction electrocatalysts based on carbon nanotubes: Mechanism and origin of ORR activity. *Energy Environ. Sci.* **2014**, *7*, 1950–1958. [[CrossRef](#)]
43. Ruiz-Cornejo, J.C.; Vivo-Vilches, J.F.; Sebastián, D.; Martínez-Huerta, M.V.; Lázaro, M.J. Carbon nanofiber-supported tantalum oxides as durable catalyst for the oxygen evolution reaction in alkaline media. *Renew. Energy* **2021**, *178*, 307–317. [[CrossRef](#)]
44. Ruiz-Cornejo, J.C.; Sebastián, D.; Pardo, J.I.; Martínez-Huerta, M.V.; Lázaro, M.J. Sulfur-doped carbon nanofibers as support for tantalum oxides bifunctional catalysts for the oxygen reduction and evolution reactions. *J. Power Sources* **2022**, *546*, 231988. [[CrossRef](#)]
45. Chen, X.; Gao, P.; Liu, H.; Xu, J.; Zhang, B.; Zhang, Y.; Tang, Y.; Xiao, C. In situ growth of iron-nickel nitrides on carbon nanotubes with enhanced stability and activity for oxygen evolution reaction. *Electrochim. Acta* **2018**, *267*, 8–14. [[CrossRef](#)]
46. Ahmed, M.S.; Begum, H.; Kim, Y.B. Iron nanoparticles implanted metal-organic-frameworks based Fe–N–C catalysts for high-performance oxygen reduction reaction. *J. Power Sources* **2020**, *451*, 227733. [[CrossRef](#)]
47. Stoerzinger, K.A.; Risch, M.; Han, B.; Shao-Horn, Y. Recent Insights into Manganese Oxides in Catalyzing Oxygen Reduction Kinetics. *ACS Catal.* **2015**, *5*, 6021–6031. [[CrossRef](#)]
48. Ramaswamy, N.; Mukerjee, S. Influence of inner- and outer-sphere electron transfer mechanisms during electrocatalysis of oxygen reduction in alkaline media. *J. Phys. Chem. C* **2011**, *115*, 18015–18026. [[CrossRef](#)]
49. Poux, T.; Bonnefont, A.; Ryabova, A.; Kéranguéven, G.; Tsirlina, G.A.; Savinova, E.R. Electrocatalysis of hydrogen peroxide reactions on perovskite oxides: Experiment versus kinetic modeling. *Phys. Chem. Chem. Phys.* **2014**, *16*, 13595–13600. [[CrossRef](#)]
50. Guan, D.; Shi, C.; Xu, H.; Gu, Y.; Zhong, J.; Sha, Y.; Hu, Z.; Ni, M.; Shao, Z. Simultaneously mastering operando strain and reconstruction effects via phase-segregation strategy for enhanced oxygen-evolving electrocatalysis. *J. Energy Chem.* **2023**, *82*, 572–580. [[CrossRef](#)]
51. Shinagawa, T.; Garcia-Esparza, A.T.; Takanabe, K. Insight on Tafel slopes from a microkinetic analysis of aqueous electrocatalysis for energy conversion. *Sci. Rep.* **2015**, *5*, 13801. [[CrossRef](#)] [[PubMed](#)]
52. Roche, I.; Chaînet, E.; Chatenet, M.; Vondrák, J. Carbon-supported manganese oxide nanoparticles as electrocatalysts for the Oxygen Reduction Reaction (ORR) in alkaline medium: Physical characterizations and ORR mechanism. *J. Phys. Chem. C* **2007**, *111*, 1434–1443. [[CrossRef](#)]
53. Park, S.; Jiang, T.; Zheng, K.; Lin, Z.; Meng, Y.; Wang, M.; Chen, J.; Chen, W. Ultrafast Thermal Synthesis of Non-Noble Metal-Based Electrocatalysts for Overall Water Splitting. *ACS Appl. Energy Mater.* **2023**, *6*, 5787–5796. [[CrossRef](#)]
54. Kapalka, A.; Fóti, G.; Comminellis, C. Determination of the Tafel slope for oxygen evolution on boron-doped diamond electrodes. *Electrochem. Commun.* **2008**, *10*, 607–610. [[CrossRef](#)]
55. Sebastián, D.; Alegre, C.; Gálvez, M.E.; Moliner, R.; Lázaro, M.J.; Aricò, A.S.; Baglio, V. Towards new generation fuel cell electrocatalysts based on xerogel-nanofiber carbon composites. *J. Mater. Chem. A* **2014**, *2*, 13713–13722. [[CrossRef](#)]
56. Xiao, X.; Zhang, W.; Zhao, H.; Li, L.; Deng, P.; Wu, Y.; Luo, S.; Chen, B. Ultrathin amorphous MnO₂ modified prawn shells-derived porous carbon towards robust oxygen electrocatalyst for rechargeable Zn-air battery. *Ceram. Int.* **2022**, *48*, 6506–6511. [[CrossRef](#)]
57. Meng, Y.; Song, W.; Huang, H.; Ren, Z.; Chen, S.Y.; Suib, S.L. Structure-property relationship of bifunctional MnO₂ nanostructures: Highly efficient, ultra-stable electrochemical water oxidation and oxygen reduction reaction catalysts identified in alkaline media. *J. Am. Chem. Soc.* **2014**, *136*, 11452–11464. [[CrossRef](#)]
58. Wahab, A.; Iqbal, N.; Noor, T.; Ashraf, S.; Raza, M.A.; Ahmad, A.; Khan, U.A. Thermally reduced mesoporous manganese MOF @reduced graphene oxide nanocomposite as bifunctional electrocatalyst for oxygen reduction and evolution. *RSC Adv.* **2020**, *10*, 27728–27742. [[CrossRef](#)]
59. Masa, J.; Xia, W.; Sinev, I.; Zhao, A.; Sun, Z.; Grütze, S.; Weide, P.; Muhler, M.; Schuhmann, W. Mn_xO_y/NC and Co_xO_y/NC nanoparticles embedded in a nitrogen-doped carbon matrix for high-performance bifunctional oxygen electrodes. *Angew. Chem. Int. Ed.* **2014**, *53*, 8508–8512. [[CrossRef](#)]
60. Gao, Y.; Zhao, H.; Chen, D.; Chen, C.; Ciucci, F. In situ synthesis of mesoporous manganese oxide/sulfur-doped graphitized carbon as a bifunctional catalyst for oxygen evolution/reduction reactions. *Carbon N. Y.* **2015**, *94*, 1028–1036. [[CrossRef](#)]
61. Gebreslase, G.A.; Sebastián, D.; Martínez-Huerta, M.V.; Lázaro, M.J. Nitrogen-doped carbon decorated-Ni₃Fe@Fe₃O₄ electrocatalyst with enhanced oxygen evolution reaction performance. *J. Electroanal. Chem.* **2022**, *925*, 116887. [[CrossRef](#)]
62. Sebastián, D.; Suelves, I.; Moliner, R.; Lázaro, M.J. The effect of the functionalization of carbon nanofibers on their electronic conductivity. *Carbon N. Y.* **2010**, *48*, 4421–4431. [[CrossRef](#)]
63. Marcano, D.C.; Kosynkin, D.V.; Berlin, J.M.; Sinitskii, A.; Sun, Z.; Slesarev, A.; Alemany, L.B.; Lu, W.; Tour, J.M. Improved synthesis of graphene oxide. *ACS Nano* **2010**, *4*, 4806–4814. [[CrossRef](#)] [[PubMed](#)]

Disclaimer/Publisher's Note: The statements, opinions and data contained in all publications are solely those of the individual author(s) and contributor(s) and not of MDPI and/or the editor(s). MDPI and/or the editor(s) disclaim responsibility for any injury to people or property resulting from any ideas, methods, instructions or products referred to in the content.